Check for updates

Visible photodetector based on transition metal-doped ZnO NRs/PEDOT:PSS hybrid materials

Xuan Hao Nguyen,[a] Hoai Nhan Luong,[bc] Hoang Anh Pham,[bc] Nhat Minh Nguyen[bc] and Vinh Quang Dang [ID] *[bcd]

A hybrid Cu-doped ZnO nanorods (ZnO:Cu NRs)/poly(3,4 ethylene dioxythiophene)-polystyrene sulfonate (PEDOT:PSS)-based photodetector was fabricated using a simple hydrothermal method with pre-patterned silver electrodes. In the hybrid structure, PEDOT:PSS with high mobility acts as a carrier transport layer, while ZnO:Cu NRs with high visible absorption works as an "antenna" material to generate electron–hole pairs under light illumination. As a result, the devices exhibits a high response in visible light at a wavelength of 395 nm. The responsivity and photoconductive gain of the hybrid photodetector reached 0.33 A W^{-1} and 1.306, respectively, which is 1.36 times higher than those of Cu-doped ZnO NRs-based ones. The response and recovery times are improved, with values of 25.21 s and 42.01 s, respectively. The development of hybrid materials for visible photodetectors enables an innovative approach for future optoelectronic devices, especially optical sensors.

Introduction

Optoelectronics is one of the technology fields that deals with applying electronic devices to detect and control light sources. Optoelectronic devices, which directly convert between electrical signals and photons, are divided into two types: light-sensitive devices and those generating photons.[1] The common light-sensitive devices are phototransistors,[2] diodes, optical fibers, photovoltaic cells,[3] *etc.* The kind that generate photons include light emitting diodes (LEDs),[4] surface-conduction electron-emitter displays (SEDs),[5] cathode ray tubes (CRTs) of televisions, digital light processing (DLP), tungsten filament lamps, *etc.* Some devices incorporate both the principles, such as liquid crystal displays (LCDs), light-dependent resistors (LDRs),[6] and optical dimming[7] and photoelectric devices.[1] Optoelectronic devices are an important part of our life. They are used for many purposes as telecommunications,[8] military services,[9] sensing, medical equipment, and science.

Photodetectors (PDs) constitute an outstanding field of optoelectronic devices. PDs convert photons or electromagnetic radiation into electrical signals. The absorbed photons generate electron–hole pairs in the active materials.[10] Depending on the properties of the materials, photodetectors operate in different light regions, such as X-rays, ultraviolet (UV), infrared, and visible. Most of the main materials in PDs are direct bandgap materials such as silicon and II–VI semiconductors.[11] Photodetectors are applied in many fields in practical life such as optical communication, biomedical imaging, security, environmental sensing, safety, optical sensors, hot engine flame detection, leak detection, and motion detection.[12]

In optical sensor applications, metal oxide nanostructures are emerging as potential semiconductors for active materials in photodetectors due to their excellent optical properties. Among them, ZnO NRs have received lots of attention from scientists thanks to their optical and electric properties. For instance, ZnO NRs possess a wide bandgap (3.27 eV), large exciton binding energy of 60 meV at room temperature, thermal stability, low cost, non-toxicity, transparency, higher optical gain, specific crystalline orientation, electrical conductivity[13,14] and varied morphology.[15] Besides, the nanorod morphology has a unique advantage with a high surface-to-volume ratio and a large surface area.[16] Indeed, the wide bandgap allows ZnO NRs to only respond to UV light (~4% of sunlight) but not to visible light, which accounts for 43% of the solar spectra, resulting in reduced performance of devices based on this material. In order to broaden the light absorption of ZnO NRs towards the visible region as well as enhance the device performance, many research studies have focused on doping transition metals in ZnO structures,[17] decorating with noble metals,[18] optimizing the ZnO structure with other materials like ZnO/ZnMgO,[19,20] or hybridizing them with active materials like PTB7:PC$_{71}$BM.[21] As for the second example, a good candidate among noble metals is silver nanoparticles (Ag NPs). In spite of chemical stability, high electrical conductivity, and strong plasmonic response,

[a] Thu Dau Mot University, Phu Hoa Ward, Thu Dau Mot City, Binh Duong Province, Vietnam

[b] Department of Materials Science and Technology, University of Science, Ward 4, District 5, Ho Chi Minh City, Vietnam. E-mail: vinhquangntmk@gmail.com

[c] Vietnam National University, Ho Chi Minh (VNU-HCM), Linh Trung Ward, Thu Duc District, Ho Chi Minh City, Vietnam

[d] Center for Innovative Materials and Architectures (INOMAR), Quarter 6, Linh Trung Ward, Thu Duc District, Ho Chi Minh City, Vietnam

depositing Ag on ZnO NRs is still difficult, thus posing challenges for the decorating method. Another good method to control the optical properties of ZnO nanorods is by doping transition elements such as Ga, In, Sn, Mn, Mg, Bi, and Al.[22] Bae et al.[23] reported that ZnO nanorods showed different emission bands, including violet and blue emission bands by the doping of Pb^{2+} into ZnO nanorods. Furthermore, when doping with copper (Cu), owing to the similar ionic radii of Zn^{2+}, Cu^{2+}, and Cu^{+}, which were 0.74 nm, 0.72 nm, and 0.96 nm, respectively, Cu^{2+} can substitute Zn^{2+} ions in the crystal lattice.[24] The impurity levels located above the valence band or below the conduction band acted as acceptor levels or donor levels, respectively, making the semiconductors responsive to visible light.[13] Although Cu-doped ZnO NRs have been used a lot in visible photodetectors, these device's performances are not high, for example, their response and recovery times are slow due to low mobility and conductivity with a fast recombination of carriers. Therefore, it is necessary to hybridize Cu-doped ZnO NRs with a carrier-transport material to overcome the aforementioned limitations as well as enhance the efficiency of the devices. Many materials have been used to make the carrier-transport layer such as graphene,[25] MoS_2,[26] and PEDOT:PSS.[27] Among them, PEDOT:PSS is a suitable material to form heterojunctions with Cu-doped ZnO NRs due to its appropriate energy band, which allow charge carriers to move easily.

In this work, visible photodetectors based on hybrid ZnO:Cu NRs/PEDOT:PSS are fabricated on glass substrates by the hydrothermal method. Ag electrodes were patterned by the sputtering process using a shadow mask. In this hybrid structure, Cu-doped ZnO NRs acts as an "antenna-substance", which absorbs visible light to generate electron–hole pairs, while a conjugated polymer PEDOT:PSS with high hole mobility stability and conductivity as high as 1–4000 S cm^{-1} (ref. 28) acts as a transport layer. Interestingly, PEDOT:PSS layer plays an important role in minimizing the trapping states on the surface and the grain boundaries of Cu-doped ZnO, which have a detrimental influence to the optoelectronic properties.[29] The morphology and structure of hybrid ZnO:Cu NRs/PEDOT:PSS are investigated by scanning electron microscopy (SEM) and X-ray diffraction (XRD), respectively; the optical property is recorded by Ultraviolet–Visible spectroscopy (UV-Vis). The photodetector performance was investigated by I–V and I–t characteristics. As a result, the hybrid photodetector exhibited an enhancement of response-ability, and the responsivity increased from 0.14 A W^{-1} to 0.33 A W^{-1}, which is 1.36 times higher than that of devices without transport materials. The photoconductive gain reached the value of 1.306. So, the hybrid ZnO:Cu NRs/PEDOT:PSS based PDs promise to improve the response and recovery times, thereby enabling a prospect of new optoelectric devices using visible light.

Experimental methods

Chemical materials

Zinc oxide nanoparticles 40 wt% dispersed in ethanol were bought from Sigma Aldrich. Poly(3,4-ethylene dioxythiophene)-polystyrene sulfonate (PEDOT:PSS), zinc nitrate hexahydrate

with purity 99% ($Zn(NO_3)_2 \cdot 6H_2O$), and hexamethylenetetramine (HTMA, $C_6H_{12}N_4$) were bought from Xilong Scientific. Copper(II) sulfate pentahydrate with purity 99% ($CuSO_4 \cdot 5H_2O$) was bought from Guangdong Guanghua Chemical Factory Co.

Synthesis process

Synthesis procedure of Cu-doped ZnO NRs. The Cu-doped ZnO NRs with various Cu loadings (Cu : Zn molar ratio) were prepared by the hydrothermal method following our previous research.[30] Firstly, PEDOT:PSS was spin-coated on a glass substrate at 3000 rpm for 30 s. Then, the substrate was annealed in air at 100 °C for 15 min. Subsequently, 2 wt% ZnO NPs in ethanol were spin-coated on PEDOT:PSS/glass substrate at 3000 rpm for 30 s, which was repeated 2 times and heated in air at 80 °C each time. Consequently, the ZnO seed layer on PEDOT:PSS/glass substrate was put into a mixed aqueous solution including 50 mM $Zn(NO_3)_2 \cdot 6H_2O$, 50 mM HTMA ($C_6H_{12}N_4$), and 10 mM $CuSO_4 \cdot 5H_2O$ at 90 °C for 4 h to grow ZnO:Cu NRs. Finally, the samples were cleaned with deionized (DI) water and dried at 100 °C for 30–60 min.

Fabrication of the photodetector

Before patterning a channel with 400 μm width and 8 mm length by Ag electrodes sputtering through a shadow mask, ZnO:Cu NRs were grown directly onto the coated PEDOT:PSS to form the hybrid channel. Because ZnO:Cu NRs acted as an n-type material and PEDOT:PSS served as a p-type semiconductor, the contact of these two materials could be considered as a p–n junction. Then, 100 nm thickness of Ag layer was controlled by a procedure of 60 s deposition with a current of 0.1 A.

Device characterization

The crystal structure of materials was investigated by X-ray diffraction (XRD) using monochromatic Cu-K$_{\alpha 1}$ radiation ($\lambda = 1.54$ Å, the jump: 0.015°, and the power 40 kV, 40 mA to 1.600 W). Measurement results were obtained from the machine D8-Advance-Bruker. The UV-Vis absorption spectra in the wavelengths from 350 to 800 nm were obtained using UV-1800-Shimadzu-Japan with the scanning rate of 0.5 nm s^{-1} and source power of 60 Hz. The excited light source was LED with a wavelength of 395 nm. The photodetector performances were recorded by I–V, I–t characteristics using Keithley 2400 machine.

Results and discussions

The scheme in Fig. 1a depicted the fabrication process and Fig. 1b showed the ultimate structure of the visible detection devices using ZnO:Cu NRs/PEDOT:PSS hybrid-channel photoresistor. Briefly, the process began with depositing the hybrid materials on a glass substrate. The channels were formed by the patterning of silver electrodes on the substrate using a shadow mask. The device dimensions were 400 μm in channel width and 8 mm in channel length. Then, the characteristics of the visible detection device were measured at room temperature and ambient conditions. The fabrication and measurement
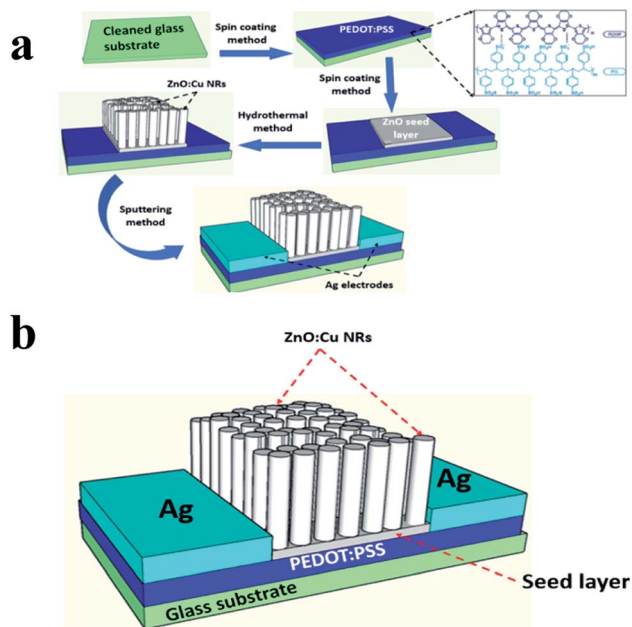
Fig. 1 (a) The fabrication process of the hybrid photodetector. (b) The ultimate structure of the device.

processes are clarified in more detail in the experimental methods.

Materials optimization

Optical properties. To examine the optical characteristics of the materials, UV-Vis absorption spectra of the undoped ZnO NRs and ZnO NRs doping with 3%, 5%, 7%, and 9% Cu in the wavelength range of 350–800 nm were investigated, as depicted in Fig. 2a. The pure ZnO NRs showed only a strong absorption band in the ultraviolet region (389 nm). Under Cu doping, the
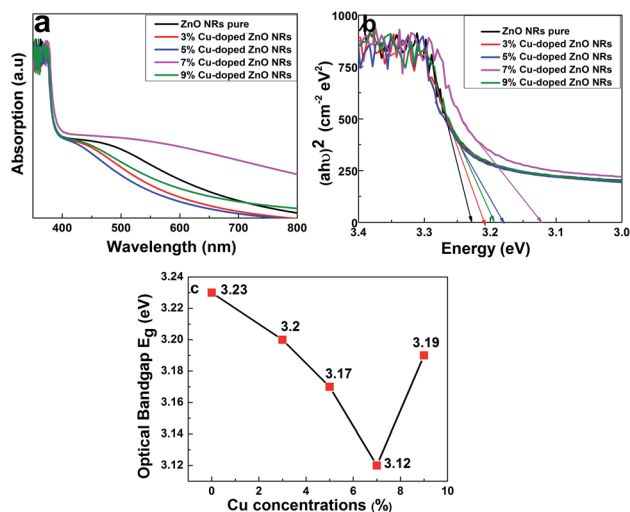
absorption edges shifted toward the visible region. It was attributed to the impurity levels in the bandgap of ZnO created by the Cu dopants, which was clearly clarified in our previous report.[30] When the Cu doping concentration increased from 3% to 7%, the absorption edges shifted to a longer wavelength region. The carrier concentration donated by interstitial zinc atoms or oxygen vacancies was reduced, which shifted the Fermi level to lower energies, thus decreasing the optical band gap values of doped ZnO NRs.[31] However, if the doping concentration further accelerated, the absorption edge shifted back toward UV light, which was explained by the Moss–Burstein effect.[31] Indeed, the Fermi level is located above the conduction band at a high doping concentration. As a result, the filling of the conduction band led to the absorption transitions between the valence band and Fermi level in the conduction band. This transition level change shifted the absorption edge to higher energies.[32] The highest shift belonged to the samples with 7% Cu doping concentration that indicated the minimum value of the optical band gap, which was calculated by the Tauc's plot method, presented in Fig. 2b and accorded to the equation[33] $(\alpha h\nu)^{1/n} = A(h\nu - E_g)$, where α, A, $h\nu$, and E_g are the absorption coefficient, relation constant, photon energy, and optical band gap, respectively. $n = 0.5$ for semiconductors with a direct band gap, and $n = 2$ with the indirect band gap. The optical band gap values of the Cu-doped ZnO NRs were 3.20 eV for 3%, 3.17 eV for 5%, 3.12 eV for 7%, and 3.19 eV for 9% doping, which were linear extrapolated from the photon energy axis (Fig. 2c). Therefore, the lowest optical band gap belonged to 7% Cu-doped ZnO NRs with the value of 3.12 eV, corresponding to the wavelength of 397 nm.

The structural properties. To determine the structure of the samples, XRD patterns were recorded. As shown in Fig. 3a, all the exhibited characteristic peaks of ZnO NRs at 2θ of 31.89°, 34.54°, 36.37°, 47.61°, 56.70°, and 62.93° which could be assigned to (100), (002), (101), (102), (110), and (103) planes, demonstrating the hexagonal wurtzite structure[34] and the substitution of Cu^{2+} did not destroy the crystal lattice in the host materials. No new peak was observed, which indicated that the Cu^{2+} well substituted the Zn^{2+}, and there was no agglomeration of Cu to form the new phases.[35] The highest peak in the (002) plane showed the priority development of ZnO NRs accorded to the c-axis. In Fig. 3b, the shift of the (002) peak at 34.54° toward the smaller 2 theta presented the successful substitution of Cu^{2+}

Fig. 2 (a) UV-Vis spectra of ZnO NRs and Cu doping at different concentrations. (b) Plot of $(\alpha h\nu)^2$ *versus* energy, and the extrapolation of the linear parts of ZnO. (c) Optical bandgap of pure and Cu-doped ZnO NRs at different concentrations.
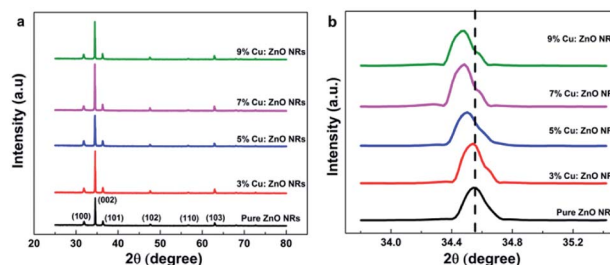

Fig. 3 (a) XRD patterns of the undoped and Cu-doped ZnO nanorods. (b) Comparison of the (002) peaks taken for pure and Cu-doped ZnO NRs at different concentrations.

with Zn^{2+}. Indeed, due to different ionic radius between Cu^{2+} (0.73 Å) and Zn^{2+} (0.74 Å), Cu^{2+} ions deformed the ZnO crystal lattice.[36] Besides, the crystallinity of materials affected the performance of photodetectors, especially their response time and recovery time. That statement is supported by the study of Nie et al.,[37] which confirmed that the high crystallinity of ZnO nanostructures with a low density of trap centers on their surfaces made their carrier mobility more excellent and led their photoresponse speed much faster. Among various doping concentrations, the highest (002) peak intensity was observed for the sample with 7% Cu doping, implying that the best crystallinity was obtained at 7% Cu doping concentration, which matched with the absorption spectra, which had been analyzed above. Furthermore, the existence and distribution of Cu in the ZnO NRs were confirmed and clearly discussed through the EDS mapping and XPS spectra in our previous papers.[30,38]

Surface morphologies. In order to confirm that the materials had a hexagonal wurtzite structure, the morphology of 7% Cu-doped ZnO NRs was investigated by scanning electron microscopy (SEM) as shown in Fig. 4. The top view SEM images in Fig. 4a showed a uniform and high density of nanorods. The average diameter of the nanorods was about 110 nm. The nanorods owned hexagonal wurtzite structure, which agreed with the XRD patterns shown in Fig. 2. Fig. 4b presented the cross-section of ZnO:Cu NRs that confirm the vertical growth onto PEDOT:PSS substrates. The length of nanorods was around 2 μm. Due to the high surface-to-volume ratio, this structure not only increased the surface area for absorbing light but also reduced the scattering of light,[39] leading to the enhancement of the hybrid device's performance.

Photodetector characteristics

Photodetector performance under visible light illumination. The optical sensors with photoresistor structure were characterized by $I–V$ and $I–t$ measurements. Fig. 5a and b presented the $I–V$ characteristics of photodetectors based on ZnO:Cu NRs with and without PEDOT:PSS layer under 395 nm light exposure. In dark conditions, the linear $I–V$ relations, which were almost symmetrical under both forward and reverse bias, indicated a good ohmic metal–semiconductor contact behavior.[40] The device with a hole transport layer showed a higher dark current than that of the device without one, which was put down to the high conductivity of the PEDOT:PSS layer. From the $I–V$ curves, it can be clearly seen that the current of the
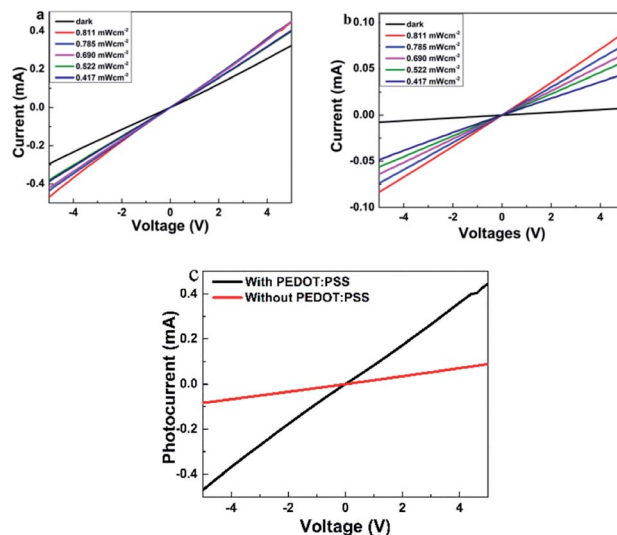
Fig. 5 $I–V$ characteristics of (a) Cu-doped ZnO NRs/PEDOT:PSS, (b) Cu-doped ZnO NRs photodetectors under 395 nm light illumination, and (c) the photocurrent of the samples with and without PEDOT:PSS under 395 nm light exposure with a photon intensity of 0.811 mW cm^{-2}.

device increased with the increasing light intensity. Both the samples with and without PEDOT:PSS showed the rise of photocurrent, with the surge belonging to the sample on PEDOT:PSS substrate (Fig. 5c). In other words, under exposure of 395 nm light intensity (P) of 0.811 mW cm^{-2} and 5 V applied bias, the photocurrent of the device with PEDOT:PSS was 0.125 mA, which was nearly 1.5 times higher than that of the sample without PEDOT:PSS (0.0823 mA). This emphasized the role of PEDOT:PSS in the devices, which is clarified in the mechanism section.

To deeply understand the performance of photodetectors, current–times ($I–t$) characteristic measurement was conducted. The time-resolved photoresponse of the photodetector with and without the transport layer at a bias of 5 V is shown in Fig. 6. Both devices showed the increase in photocurrent under visible light illumination and the decay ability when the light was turned off. It was attributed to the generation of electron–hole pairs under light exposure. Indeed, when ZnO:Cu NRs absorbed the photons with an energy higher than the optical band gap, valence electrons lifted to the conduction band to become the conductance electrons and left behind the holes in the valence
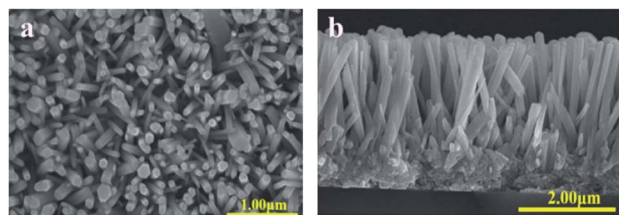
Fig. 4 SEM images of Cu-doped ZnO NRs/PEDOT:PSS: (a) the top view, (b) the cross-section.
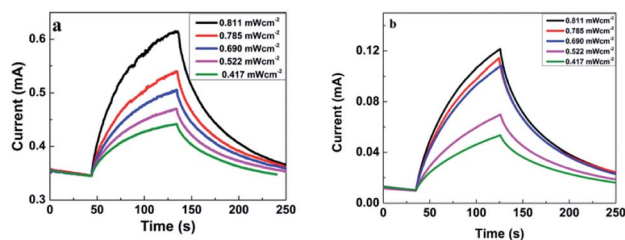
Fig. 6 Time-resolved photocurrent response under 395 nm illumination with 5 V bias of the devices (a) with PEDOT:PSS and (b) without PEDOT:PSS.

band. Consequently, electron–hole pairs were generated inside ZnO:Cu NRs leading to the increase in the photocurrent, which is discussed in more detail in the mechanism part. With different light intensities, the photocurrent values went up when P climbed (Fig. 6a and b). This result is explained by the relationship between photocurrent and light intensity,[41] $I_{photo} = AP^{\theta}$, where A is the wavelength constant and θ is the exponential. At an incident illumination of 0.811 mW cm^{-2}, the photocurrent reached 0.269 mA for the sample with PEDOT:PSS, while the corresponding value without hole transport layer was 0.110 mA. This matched with the I–V characteristic, which has been given above.

Two important parameters in a photodetector are responsivity (R) and photoconductive gain (G). Therefore, to determine the device performance, R and G should be calculated from I–V and I–t curves. The responsivity was defined by the ratio of generated photocurrent to illumination intensity, and it could be calculated using the formula[42]

$$R = \frac{I_{ph}}{P}$$

where $I_{ph} = I_{light} - I_{dark}$ was photocurrent, I_{light} was the current under illumination, I_{dark} was the current without light, and P was the incident light intensity. The photoconductive gain, which was defined as the ratio between the number of electrons collected per incident photon, was determined from the equation.[43,44]

$$G = \frac{hc}{\lambda\,e} R = \frac{\tau_{life} \times \mu \times V_{bias}}{L^2}$$

where h was Planck's constant, c represented the velocity of light, 3×10^8 ms^{-1}, λ was the light wavelength, e was the electron charge, and R was the responsivity of the photodetector, τ_{life} was the lifetime, μ: mobility of carriers, and L was the distance between electrodes. Under the same illuminating condition (wavelength of 395 nm and light intensity of 0.811 mW cm^{-2}), the responsivity of the device with hole transport layer was 0.33 A W^{-1}, nearly 2.36 times higher than that without transport layer (0.14 A W^{-1}). The photoconductive gain of the device with PEDOT:PSS was 1.036, a twofold value compared to that without PEDOT:PSS (0.439) (Table 1). One explanation was that G depended on the charge carrier mobility, and thus, the higher the mobility, the higher the photoconductive gain.[43,44]

Fig. 7a presents the response time and recovery time of the photodetector based on ZnO:Cu NRs with and without PEDOT:PSS. Following other reports, response time was defined as the time to reach 63% of the photocurrent response from the start of the illumination, while recovery time was calculated as the time to reach 37% of photocurrent after turning off the light.[45,46] The hybrid photodetector exhibited a response time of 28.21 s, faster than that of Cu-doped ZnO NRs (36.41 s). This was because the mobility of PEDOT:PSS was higher than that of ZnO:Cu NRs. To investigate the stability of the device, the reversible switching between high and low currents was denoted in Fig. 7b, where the incident light was turned on and off repeatedly. It could be clearly seen that slight changes in sensing performance after four repetitions of switching between the light on and off state demonstrated good stability of our device.

Photodetection mechanism. The increase in the current under visible light could be clarified by the following two sensing mechanisms, which are the photovoltage effect and photogating effect. Regarding the photovoltage effect, the pre-contact energy band diagrams of ZnO:Cu NRs and PEDOT:PSS relative to vacuum levels are qualitatively outlined in Fig. 8a, where their χ electron affinities were 4.3 and 3.6 eV,[47,48] correspondingly. The difference between the two energy gaps induced a conduction-band discontinuity ΔE_C and a valence-band discontinuity ΔE_V, corresponding to the energetic barrier for electrons and holes, respectively. Under dark conditions, the contact of ZnO:Cu NRs with the PEDOT:PSS layer formed a local p–n junction at the interface between
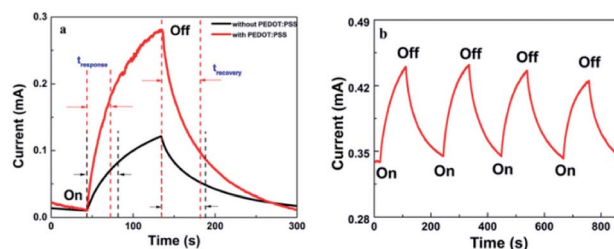

Fig. 7 I–t curves of the device (a) with and without PEDOT:PSS in 1 cycle, and (b) with PEDOT:PSS in 4 continuous cycles.

Table 1 The summary of our research results and comparison of the performance of our PDs with various ZnO NRs structure PDs

Active materials	λ (nm)	I_{ph} (mA)	Response time (s)	Recovery time (s)	R (A W^{-1})	Bias	Reference
ZnO NRs	365	0.36	25.74	36.73	0.87	5	56
ZnO NRs	365	0.308	38.10	3.66	—	—	57
Cu-doped ZnO NRs	380	0.89	58	83	—	3	39
Mn doped ZnO NRs/PEDOT:PSS	365	—	2.75	16.8	0.065	5	58
ZnO@CdS/PEDOT:PSS	470	1.4×10^{-3}	~0.02	~0.02	—	0	59
AZO/ZnO/PVK/PEDOT:PSS	365	—	0.11	0.2	0.081	5	60
ZnO NRs/GQD/PEDOT:PSS	340	~15	—	—	36	−1	28
Single crystal ZnO/PEDOT:PSS	370	3.5×10^{-6}	—	—	0.3	—	61
Cu-doped ZnO NRs	395	0.1145	36.41	48.3	0.14	5	This work
Cu-doped ZnO NRs/PEDOT:PSS	395	0.2704	28.21	42.01	0.33	5	This work
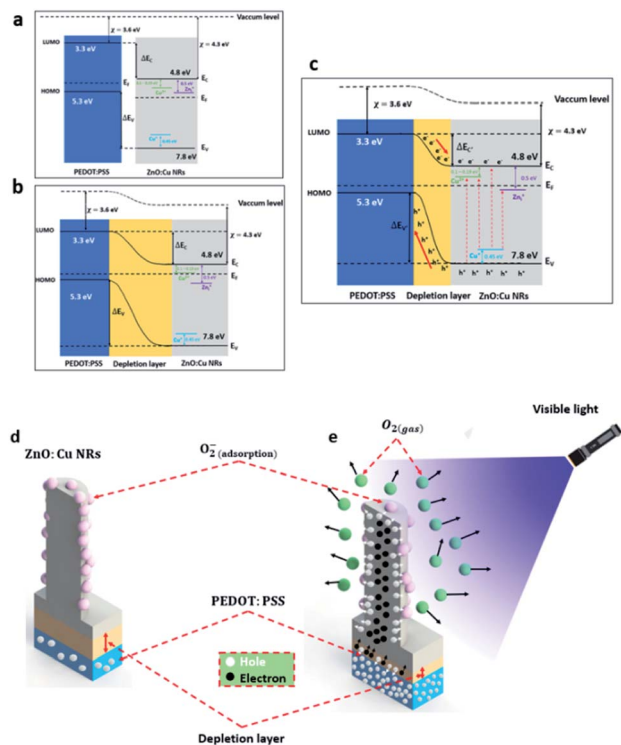
Fig. 8 (a) The energy diagram of ZnO:Cu NRs and PEDOT:PSS before contact. (b) Schematic illustration of the energy band structure of ZnO:Cu NRs/PEDOT:PSS heterojunction in dark conditions. (c) The electron–hole pair generation and transmission process under visible illumination. The schematic diagram of the visible photodetector with the ZnO:Cu NRs/PEDOT:PSS heterojunction (d) under dark conditions and (e) visible illumination.

ZnO:Cu NRs and PEDOT:PSS. This enabled a charge depletion layer at the interface, and an integration potential (ΔE_C) was formed inside the depletion layer (Fig. 8b). At the same time, oxygen molecules from the ambient air were absorbed on the surface of the nanorods by capturing free electrons.[49,50] They reduced the mobility of the carriers, creating a depletion region near the surface, according to equation[51] (Fig. 8d), $[O_{2(gas)} + e^- \rightarrow O_2^-{}_{(adsorption)}]$. As known, the work function of PEDOT:PSS was higher than that of ZnO:Cu NRs[52] as shown in Fig. 8b and c. Under visible light radiation, the electron–hole pairs were generated in the depletion layer thanks to ΔE_C (ΔE_C acts as the driving force to separate the electron–hole pairs generated inside the depletion layer under excitation of near-visible light).[53] The electrons could not move towards PEDOT:PSS due to the ΔE_C barrier, but drive towards the ZnO NRs. Meanwhile, electrons reduced the built-in potential from ΔE_C to $\Delta E_{C'}$ and the holes moved towards PEDOT:PSS. Therefore, the width of the depletion layer was narrowed and the electron transport channel was enlarged, leading to an increase in the PEDOT:PSS channel's conductance (Fig. 8c and e). For photogating effect, in the dark condition, the depletion layer was formed at the interface between ZnO:Cu NRs and PEDOT:PSS due to the different work functions of the two materials (Fig. 9a). Under visible light illumination, electrons from the valence band of ZnO NRs could be easily excited up to the conduction band
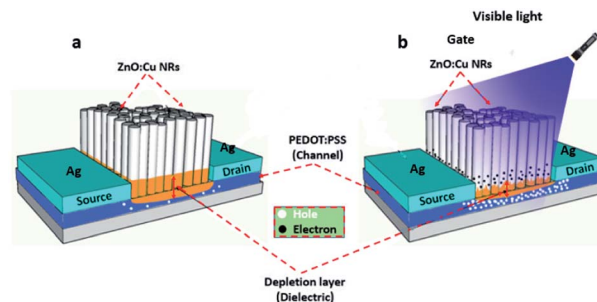
Fig. 9 Schematic diagrams of the visible photodetector considered as a vertical transistor with a photogating effect under (a) dark conditions and (b) light illumination.

owing to the intermediate energy levels of Cu dopant, resulting in the generation of electron–hole pairs inside ZnO NRs[30,51] (Fig. 9b) $[h\nu \rightarrow e^- + h^+]$. The photoexcited holes were trapped by the adsorbed O_2^-, releasing oxygen molecules from the surface of nanorods, as presented in equation[30] and Fig. 8e, $[O_2^-{}_{(ad)} + h^+ \rightarrow O_{2(gas)}]$. Simultaneously, electrons were trapped inside the ZnO:Cu NRs, leading to the formation of a negative potential near the depletion layer. That made the additional negative potential inside the ZnO NRs, which effectively gated the PEDOT:PSS channel through capacitive coupling. As a result, the holes inside the PEDOT:PSS are accumulated at a high density, thereby increasing the optical current of the device.[53] Our device operated according to a combination of photo-voltage and photogating effects in which the ZnO NRs acted as a photo-responsive gate, the PEDOT:PSS acted as the channel, the depletion layer serves as a dielectric, and Ag electrodes play the role of source-drain electrodes. Fig. 9a showed a schematic illustration of the device in dark conditions ($V_G = 0$). Fig. 9b depicted the device under visible light illumination ($V_G < 0$) when a photovoltage effect was created at the PEDOT:PSS/ZnO NRs interface to control the electrostatics of the depletion layer, and the photogating effect was generated inside the ZnO NRs to gate the PEDOT:PSS channel.

Comparing the performance of these PDs to the different research studies, the proposed device showed superior performances of photocurrent and responsivity. As shown in Table 1, the values of response time, recovery time, R, and G have been enhanced. Thus, the structure of this device has reached the theoretical suggestions. In addition, the response and recovery times of the device can be improved by boosting either the crystallinity of ZnO nanorods[54] or the mobility of the carrier transport layer,[55] which will be conducted in our following study. Although the performance of our device was relatively low, it was still higher than that in some other reports, which meant that our results were acceptable for some realistic applications.

Conclusions

In summary, we successfully synthesized a hybrid material between Cu-doped ZnO NRs and PEDOT:PSS on a glass substrate. The performance of the hybrid photodetector was enhanced due to the high mobility of the hole transport layer.

With 7% Cu doping, the hybrid photodetector responded to the visible light with a wavelength of 395 nm. The responsivity of the hybrid photodetector was 0.33 A W^{-1}, higher than that of ZnO:Cu NRs photodetector (0.14 A W^{-1}). The device with the transport layer also showed fast response and recovery times with values of 28.21 s and 42.01 s, respectively. These suggest that our device has the potential for further applications in the future.

Conflicts of interest

There are no conflicts to declare.

Acknowledgements

Notes and references

1 J. Haas, M. Schwartz, U. Rengstl, M. Jetter, P. Michler and B. Mizaikoff, *Analyst*, 2018, **143**, 593–605.

2 F. Li, C. Ma, H. Wang, W. Hu, W. Yu, A. D. Sheikh and T. Wu, *Nat. Commun.*, 2015, **6**, 1–8.

3 Y. Cui, H. Yao, L. Hong, T. Zhang, Y. Xu, K. Xian, B. Gao, J. Qin, J. Zhang and Z. Wei, *Adv. Mater.*, 2019, **31**, 1808356.

4 Z. Zhou, Y. Li, M. Xia, Y. Zhong, N. Zhou and H. T. Hintzen, *Dalton Trans.*, 2018, **47**, 13713–13721.

5 K. Yamamoto, T. Oguchi, K. Sasaki, I. Nomura, S. Uzawa and K. Hatanaka, *J. Soc. Inf. Disp.*, 2006, **14**, 73–79.

6 X.-Y. Wang, A. L. Fitch, H. H. C. Iu, V. Sreeram and W.-G. Qi, *Chin. Phys. B*, 2012, **21**, 108501.

7 H. M. Günther, T. Birnstiel, D. P. Huenemoerder, D. A. Principe, P. C. Schneider, S. J. Wolk, F. Dubois, L. Logie, S. Rau and S. Vanaverbeke, *Astron. J.*, 2018, **156**, 56.

8 P. Ma, N. Flöry, Y. Salamin, B. Baeuerle, A. Emboras, A. Josten, T. Taniguchi, K. Watanabe, L. Novotny and J. Leuthold, *ACS Photonics*, 2018, **5**, 1846–1852.

9 R. D. Hudson and J. W. Hudson, *Proc. IEEE*, 1975, **63**, 104–128.

10 Z. Zhao, J. Liu, Y. Liu and N. Zhu, *J. Semicond.*, 2017, **38**, 121001.

11 F. Huang, F. Jia, C. Cai, Z. Xu, C. Wu, Y. Ma, G. Fei and M. Wang, *Sci. Rep.*, 2016, **6**, 28943.

12 S. Youssef, Y. M. El-Batawy and A. A. Abouelsaood, *J. Appl. Phys.*, 2016, **120**, 124506.

13 M. Wang, F. Ren, G. Cai, Y. Liu, S. Shen and L. Guo, *Nano Res.*, 2014, **7**, 353–364.

14 M. W. Zhu, N. Huang, J. Gong, B. Zhang, Z. J. Wang, C. Sun and X. Jiang, *Appl. Phys. A*, 2011, **103**, 159–166.

15 A. Bera and D. Basak, *Appl. Phys. Lett.*, 2009, **94**, 163119.

16 M. Chakraborty, A. Ghosh and R. Thangavel, *J. Sol-Gel Sci. Technol.*, 2015, **74**, 756–764.

17 D. Li, Z. T. Liu, Y. H. Leung, A. B. Djurišić, M. H. Xie and W. K. Chan, *J. Phys. Chem. Solids*, 2008, **69**, 616–619.

18 J. Lermé, *J. Phys. Chem. C*, 2011, **115**, 14098–14110.

19 A. K. Dikshit, S. Maity, N. Mukherjee and P. Chakrabarti, *IEEE J. Photovolt*, 2021, **11**, 983–990.

20 S. Maity, B. Das, R. Maity, N. P. Maity, K. Guha and K. Srinivasa Rao, *Sol. Energy*, 2019, **185**, 439–444.

21 S. Maity and T. Thomas, *IEEE Trans. Electron Devices*, 2018, **65**, 4548–4554.

22 Y. Li, G. W. Meng, L. D. Zhang and F. Phillipp, *Appl. Phys. Lett.*, 2000, **76**, 2011–2013.

23 S. Y. Bae, C. W. Na, J. H. Kang and J. Park, *J. Phys. Chem. B*, 2005, **109**, 2526–2531.

24 A. Ghosh, A. Ghule and R. Sharma, *J. Phys.: Conf. Ser.*, 2012, **365**, 012022.

25 X. Zhang, J. Zhang, B. Leng, J. Li, Z. Ma, W. Yang, F. Liu and B. Liu, *Adv. Mater. Interfaces*, 2019, **6**, 1901365.

26 K.-L. Chu, C.-H. Chen, S.-W. Shen, C.-Y. Huang, Y.-X. Chou, M.-Y. Liao, M.-L. Tsai, C.-I. Wu and C.-C. Chueh, *Chem. Eng. J.*, 2021, **422**, 130112.

27 X. Zhang, J. Li, W. Yang, B. Leng, P. Niu, X. Jiang and B. Liu, *ACS Appl. Mater. Interfaces*, 2019, **11**, 24459–24467.

28 S. Dhar, T. Majumder and S. P. Mondal, *ACS Appl. Mater. Interfaces*, 2016, **8**, 31822–31831.

29 C. Xie and F. Yan, *J. Mater. Chem. C*, 2018, **6**, 1338–1342.

30 C. H. N. Van, H. K. Nguyen, H. Q. Huynh, H. A. Pham, T. M. Dinh, H. N. Luong, B. T. Phan, C. K. Tran and V. Q. Dang, *Adv. Nat. Sci: Nanosci. Nanotechnol.*, 2020, **11**, 015002.

31 N. R. Yogamalar and A. Chandra Bose, *Appl. Phys. A*, 2011, **103**, 33–42.

32 Z. Banu Bahşi and A. Y. Oral, *Opt. Mater.*, 2007, **29**, 672–678.

33 B. D. Viezbicke, S. Patel, B. E. Davis and D. P. Birnie, *Phys. Status Solidi B*, 2015, **252**, 1700–1710.

34 Y. Ji, U. Jung, Z. Xian, D. Kim, J. Yu and J. Park, *Sens. Actuators, A*, 2020, **304**, 111876.

35 K. Omri, A. Bettaibi, K. Khirouni and L. El Mir, *Phys. B*, 2018, **537**, 167–175.

36 F. Yang, S. Ma, X. Zhang, M. Zhang, F. Li, J. Liu and Q. Zhao, *Superlattices Microstruct.*, 2012, **52**, 210–220.

37 B. Nie, J.-G. Hu, L.-B. Luo, C. Xie, L.-H. Zeng, P. Lv, F.-Z. Li, J.-S. Jie, M. Feng, C.-Y. Wu, Y.-Q. Yu and S.-H. Yu, *Small*, 2013, **9**, 2872–2879.

38 H. Q. Huynh, K. N. Pham, B. T. Phan, C. K. Tran, H. Lee and V. Q. Dang, *J. Photochem. Photobiol., A*, 2020, **399**, 112639.

39 Y.-L. Chu, L.-W. Ji, H.-Y. Lu, S.-J. Young, I.-T. Tang, T.-T. Chu, J.-S. Guo and Y.-T. Tsai, *J. Electrochem. Soc.*, 2020, **167**, 027522.

40 M. Salah, S. Azizi, A. Boukhachem, C. Khaldi, M. Amlouk and J. Lamloumi, *J. Mater. Sci.*, 2017, **52**, 10439–10454.

41 H. Zhang, X. Zhang, C. Liu, S.-T. Lee and J. Jie, *ACS Nano*, 2016, **10**, 5113–5122.

42 H. N. Pham, M. H. Tong, H. Q. Huynh, H. D. Phan, C. K. Tran, B. T. Phan and V. Q. Dang, *Sens. Actuators, A*, 2020, **311**, 112085.

43 Z. Bai, X. Chen, X. Yan, X. Zheng, Z. Kang and Y. Zhang, *Phys. Chem. Chem. Phys.*, 2014, **16**, 9525–9529.

44 Z. Bai, X. Yan, X. Chen, H. Liu, Y. Shen and Y. Zhang, *Curr. Appl. Phys.*, 2013, **13**, 165–169.

45 S. Sarkar and D. Basak, *Appl. Phys. Lett.*, 2013, **103**, 041112.

46 L. Zhu, Q. Dai, Z.-F. Hu, X.-Q. Zhang and Y.-S. Wang, *Opt. Lett.*, 2011, **36**, 1821–1823.

47 Y. Zhang, J. Xu, S. Shi, Y. Gao, X. Zhao, C. Wei, X. Zhang and L. Li, *Nanotechnology*, 2017, **28**, 415202.

48 C. S. Pathak, J. P. Singh and R. Singh, *Curr. Appl. Phys.*, 2015, **15**, 528–534.

49 V. Q. Dang, T. Q. Trung, D.-I. Kim, L. T. Duy, B.-U. Hwang, D.-W. Lee, B.-Y. Kim, L. D. Toan and N.-E. Lee, *Small*, 2015, **11**, 3054–3065.

50 V. Q. Dang, T. Q. Trung, L. T. Duy, B.-Y. Kim, S. Siddiqui, W. Lee and N.-E. Lee, *ACS Appl. Mater. Interfaces*, 2015, **7**, 11032–11040.

51 Z. Xian-Li and Z. Rong, *Chin. Phys. B*, 2015, **24**, 107703.

52 A. Kumar, S. Ratan, D. K. Jarwal, A. K. Mishra, C. Kumar, A. P. Singh, B. Mukherjee and S. Jit, *Mater. Res. Express*, 2019, **6**, 115514.

53 T. Q. Trung, V. Q. Dang, H.-B. Lee, D.-I. Kim, S. Moon, N.-E. Lee and H. Lee, *ACS Appl. Mater. Interfaces*, 2017, **9**, 35958–35967.

54 B. Nie, J.-G. Hu, L.-B. Luo, C. Xie, L.-H. Zeng, P. Lv, F.-Z. Li, J.-S. Jie, M. Feng and C.-Y. Wu, *Small*, 2013, **9**, 2872–2879.

55 S. A. Rutledge and A. S. Helmy, *J. Appl. Phys.*, 2013, **114**, 133708.

56 N. A. Hammed, A. A. Aziz, A. I. Usman and M. A. Qaeed, *Ultrason. Sonochem.*, 2019, **50**, 172–181.

57 F. Yi, Q. Liao, X. Yan, Z. Bai, Z. Wang, X. Chen, Q. Zhang, Y. Huang and Y. Zhang, *Physica E Low Dimens. Syst. Physica E Low Dimens. Syst. Nanostruct.*, 2014, **61**, 180–184.

58 C. O. Chey, X. Liu, H. Alnoor, O. Nur and M. Willander, *Phys Status Solidi Rapid Res Lett .*, 2015, **9**, 87–91.

59 S. Sarkar and D. Basak, *ACS Appl. Mater. Interfaces*, 2015, **7**, 16322–16329.

60 X. Zhang, J. Li, W. Yang, B. Leng, P. Niu, X. Jiang and B. Liu, *ACS Appl. Mater. Interfaces*, 2019, **11**, 24459–24467.

61 M. Nakano, T. Makino, A. Tsukazaki, K. Ueno, A. Ohtomo, T. Fukumura, H. Yuji, S. Akasaka, K. Tamura, K. Nakahara, T. Tanabe, A. Kamisawa and M. Kawasaki, *Appl. Phys. Lett.*, 2008, **93**, 123309.